

A Radio Map Approach for Antenna Pattern Calibration in Low-Altitude Air-to-Ground Sensing

Yuanshuai Zheng, Hao Sun, Bowen Li, Mu Jia, and Junting Chen

School of Science and Engineering, Shenzhen Future Network of Intelligence Institute (FNii-Shenzhen), and

Guangdong Provincial Key Laboratory of Future Networks of Intelligence

The Chinese University of Hong Kong, Shenzhen, Guangdong 518172, P.R. China

Abstract—Reconstructing antenna radiation patterns typically requires specialized anechoic or reverberation chambers, which are costly and resource-intensive. This paper investigates the feasibility of using outdoor signal strength measurements to achieve the same goal. Current methods relying on controlled environments are less accessible for extensive use, often requiring sophisticated instruments. To address these limitations, we propose a approach that leverages sparse reference signal received power (RSRP) measurements to build a two-dimensional (2D) power angular map (PAM) of the antenna. Assuming horizontal isotropy of the antenna, the PAM is constructed with distances as column indices and elevation angles as row indices, capturing key characteristics of the antenna's radiation pattern. A weighted K-Nearest Neighbors (KNN)-based matrix completion method is employed to impute missing values, followed by Singular Value Decomposition (SVD) to separate antenna gain from path loss. Our experimental results, obtained through simulations and real-world measurements, demonstrate that only 30 elevation angle measurements are needed to achieve a normalized mean squared error (NMSE) of less than 0.01 for the reconstructed antenna pattern of a half-wave dipole antenna. Further validation using a UAV measurement system for the VERT 2450 antenna shows that the reconstructed radiation pattern has a similar distribution to that provided in the VERT 2450 datasheet, confirming the effectiveness of our approach.

Index Terms—Antenna radiation pattern reconstruction, Power angular map, weighted KNN-based matrix completion, SVD

I. INTRODUCTION

The reconstruction of antenna radiation patterns are crucial for optimizing wireless communication systems, radar, and various electromagnetic applications. Traditional methods, such as the use of anechoic chambers (ACs) [1], [2], provide a controlled environment to eliminate multipath interference, thus enabling precise measurements of antenna radiation patterns. However, these chambers are often prohibitively expensive and impractical for widespread or rapid deployment.

Junting Chen is the corresponding author. The work was supported in part by the Basic Research Project No. HZQB-KCZY2021067 of Hetao Shenzhen-HK S&T Cooperation Zone, by the National Science Foundation of China under Grant No. 62171398 and No. 62293482, by the Shenzhen Science and Technology Program under Grant No. JCYJ20220530143804010, No. KQTD20200909114730003, and No. KJZD20230923115104009, by Guangdong Research Projects No. 2019QN01X895, No. 2017ZT07X152, and No. 2019CX01X104, by the Shenzhen Outstanding Talents Training Fund 202002, by the Guangdong Provincial Key Laboratory of Future Networks of Intelligence (Grant No. 2022B121010001), by the National Key R&D Program of China with grant No. 2018YFB1800800, and by the Key Area R&D Program of Guangdong Province with grant No. 2018B030338001.

Consequently, there is a growing need for alternative methods that can achieve comparable accuracy in less controlled environments.

Existing techniques for antenna pattern reconstruction can be broadly categorized based on their measurement environments and methodologies. One significant category involves the use of reverberation chambers (RCs). RCs have been demonstrated to be effective for measuring antenna radiation efficiency and diversity gain [3]–[5]. Despite their usefulness, RCs face challenges in accurately measuring radiation patterns due to multipath interference. Techniques such as deconvolution have been employed to reconstruct radiation patterns in non-anechoic environments, making it possible to measure patterns directly in an RC under certain conditions [6]. Another method involves using the self-correlation coefficient of the antenna pattern, which can be measured within an RC, although this still requires access to an RC [3].

Other existing techniques focus on specific types of antennas or measurement setups. For instance, the reconstruction of radiation patterns for phased-array antennas has been studied extensively, with methods assuming noise-free and uniformly generated patterns [7]. However, these approaches often lack real-world applicability due to the absence of actual measurements. In planar near-field measurement systems, clustering analysis and Voronoi cell classification have been used to achieve regional interpolation of antenna patterns, but these methods necessitate sophisticated setups like microwave anechoic chambers with robotic arms and absorbing materials [1]. Spherical vector wave techniques have been applied to reconstruct radiation patterns in spherical antenna measurements, using coordinate translation and rotational phase shift techniques to address location constraints [8].

Can we reconstruct antenna radiation patterns without the use of specialized ACs or RCs, but instead rely on outdoor signal strength measurements? The potential for this approach lies in its significant cost savings. By eliminating the need for intricately designed measurement chambers and sophisticated instruments, we can significantly reduce the costs of traditional indoor setups. Outdoor settings remove the necessity for controlled environments, making the process more accessible and cost-effective. However, outdoor measurements face challenges such as signal obstruction by buildings, vegetation, and other environmental factors, which introduce variability and

noise, complicating accurate pattern reconstruction. Additionally, outdoor measurements are often limited by the availability of line-of-sight (LOS) data. Because measurement locations are discrete, the number of LOS measurements may be further restricted.

To address these issues, this paper employs sparse reference signal received power (RSRP) measurements to construct a 2D power angular map (PAM) for antenna pattern reconstruction. Assuming that the antenna is horizontally isotropic, the PAM of the antenna is a matrix where the column indices represent distances and the row indices denote elevation angles of the antenna. The PAM captures the essential characteristics of the antenna's radiation pattern, specifically focusing on the vertical plane. we employ a modified weighted K -Nearest Neighbors (KNN)-based matrix completion method to impute the missing values, generating a more comprehensive PAM. Subsequently, we utilize singular value decomposition (SVD) to decompose the PAM. The SVD decomposition allows us to separate the antenna gain from the path loss, facilitating a simpler and cost-effective reconstruction of the antenna pattern. Experiments were conducted in both simulations and real-world systems. The numerical results show that only 30 measurements of elevation angles are required to achieve an normalized mean squared error (NMSE) of less than 0.01 for the reconstructed antenna gain. To further validate the performance of the proposed scheme, we set up a unmanned aerial vehicle (UAV) measurement system for field measurements and reconstructed the radiation pattern of the VERT 2450 antenna, which exhibited a similar distribution to the antenna radiation pattern provided in the VERT 2450 datasheet.

II. SYSTEM MODEL

A. Environment Model

Consider a scenario where a UAV equipped with a single antenna communicates with a transmitter, also equipped with a single antenna. The UAV collects RSRP measurements in the air to construct the relative antenna pattern between the UAV and the transmitter. The signal propagation path are likely to be blocked by tall buildings even though the transmitter is placed on the top of some buildings for more line-of-sight (LOS) opportunities.

Denote the UAV position as $\mathbf{x} = (x_1, x_2, x_3) \in \mathbb{R}^3$ and the location of the transmitter as $\mathbf{u} = (u_1, u_2, u_3) \in \mathbb{R}^3$. A Cartesian coordinate system is established as shown in Fig. 1. The origin is set at \mathbf{u} while the x -axis and y -axis are on the ground, and the z -axis points upward.

The antennas on the UAV and the transmitter are assumed to be horizontally isotropic. Therefore, one only needs to focus on the elevation angle of the transmitter. The elevation angle denoted as ϕ is defined as

$$\phi(\mathbf{x}) = \begin{cases} \arctan\left(\frac{\sqrt{(x_1-u_1)^2+(x_2-u_2)^2}}{x_3-u_3}\right) & \text{if } x_3 \neq u_3 \\ \pi/2 & \text{otherwise} \end{cases} \quad (1)$$

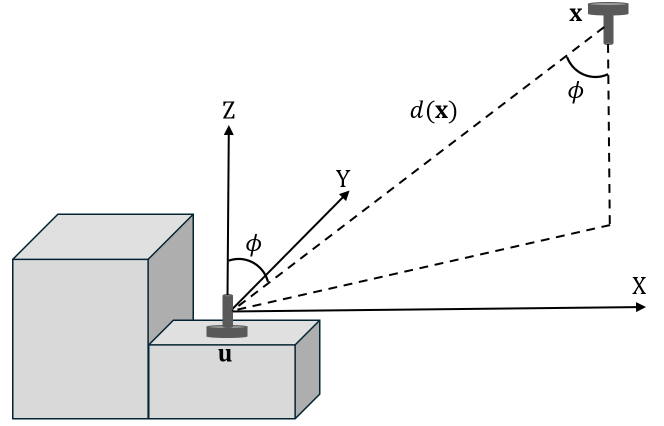


Figure 1. Measurement model for antenna pattern calibration.

which captures the angle from the positive direction of the z -axis to the negation direction of the z -axis as shown in Fig. 1. The range of ϕ is $[0, \pi]$.

B. Channel Model

Denote \mathcal{D}_0 as the set of permissible UAV positions \mathbf{x} such that there is an LOS link between the UAV and the transmitter. Denote the transmit power of the transmitter as P_t , and the channel gain from the transmitter to the UAV as $g(\mathbf{x})$. Specifically, $g(\mathbf{x})$ is modeled as

$$g(\mathbf{x}) = \begin{cases} \alpha_0 + \beta_0 \log_{10}(\|\mathbf{x} - \mathbf{u}\|_2) + \xi_0 & \text{if } \mathbf{x} \in \mathcal{D}_0 \\ \alpha_1 + \beta_1 \log_{10}(\|\mathbf{x} - \mathbf{u}\|_2) + \xi_1 & \text{otherwise} \end{cases} \quad (2)$$

where α_0 and β_0 denote the LOS channel parameters, α_1 and β_1 denote the non-line-of-sight (NLOS) channel parameters, and ξ_0 and ξ_1 capture the shadowing for LOS link and NLOS link, respectively.

The RSRP is then obtained as

$$\gamma(\mathbf{x}, \phi(\mathbf{x})) = P_t + (a_t(\phi(\mathbf{x})) + a_r(\phi(\mathbf{x}))) + g(\mathbf{x}) \quad (3)$$

where $a_t(\phi(\mathbf{x}))$ is the antenna gain of the transmitter at the elevation angle $\phi(\mathbf{x})$, and $a_r(\phi(\mathbf{x}))$ is the antenna gain of the receiver at the elevation angle $\phi(\mathbf{x})$.

Introducing $a(\phi(\mathbf{x})) \triangleq a_t(\phi(\mathbf{x})) + a_r(\phi(\mathbf{x}))$ as the relative antenna gain in the elevation angle $\phi(\mathbf{x})$, the RSRP in (3) is simplified to

$$\gamma(\mathbf{x}, \phi(\mathbf{x})) = P_t + a(\phi(\mathbf{x})) + g(\mathbf{x}). \quad (4)$$

The channel model in (2) can also be expressed as $g(d(\mathbf{x}))$ where $d(\mathbf{x}) = \|\mathbf{x} - \mathbf{u}\|_2$. Hence, the RSRP model in (4) can also be formulated in a linear form as

$$\gamma_1(d(\mathbf{x}), \phi(\mathbf{x})) = p_t \cdot a_1(\phi(\mathbf{x})) \cdot g_1(d(\mathbf{x})) \quad (5)$$

where $p_t = 10^{P_t/10}$, $a_1(\phi(\mathbf{x})) = 10^{a(\phi(\mathbf{x}))/10}$, and $g_1(d(\mathbf{x})) = 10^{g(d(\mathbf{x}))/10}$.

C. Power Angular Map

Inspired by the RSRP model in (5), we define the PAM as $\Gamma \in \mathbb{R}^{N \times M}$ where each element of Γ is the RSRP value measured at the distance $d(\mathbf{x})$ and the elevation angle $\phi(\mathbf{x})$.

Specifically, $\Gamma \in \mathbb{R}^{N \times M}$ is defined as

$$\Gamma = \begin{bmatrix} \gamma_1(d_1, \phi_1) & \dots & \gamma_1(d_M, \phi_1) \\ \vdots & \ddots & \vdots \\ \gamma_1(d_1, \phi_N) & \dots & \gamma_1(d_M, \phi_N) \end{bmatrix} \quad (6)$$

where $\{d_1, d_2, \dots, d_M\}$ is a monotonically increasing arithmetic sequence representing the distances between the UAV and the transmitter, and $\{\phi_1, \phi_2, \dots, \phi_N\}$ is another monotonically increasing arithmetic sequence representing the elevation angles. Hence, the element of the n th row and the m th column in Γ is given by $\Gamma_{nm} = p_t \cdot g_1(d_m) \cdot a_1(\phi_n)$.

The PAM defined in (6) is a sparse representation of RSRP maps. Unlike the common radio maps mapping location information to channel information such as RSRP, signal-to-noise ratio (SNR), and signal-to-interference-and-noise ratio (SINR) etc, the PAM does not require specific location information.

Remark: The PAM matrix Γ can also be a tensor which incorporates the characteristics of RSRP with respect to (w.r.t.) the azimuth angle. For each azimuth angle, the PAM is still a 2D matrix, which represents the characteristics of antenna gain and channel gain on a 2D plane perpendicular to the ground. Similarly, one can use the techniques developed in this paper to extract the antenna pattern.

III. PAM-DRIVEN ANTENNA PATTERN RECONSTRUCTION

This section first discusses the construction of the PAM from sparse measurements or existing radio maps, and then utilizes the weighted KNN-based matrix completion method to patch the PAM matrix Γ . Then, a scheme of antenna pattern reconstruction using PAM is developed.

A. PAM Construction

According to the definition of PAM matrix Γ in (6), it requires the RSRP values from M distances and N elevation angles to construct an PAM. The common radio maps use locations as indices of the channel information. For example, the common RSRP radio maps have a structure as

$$\mathcal{M} = \{(\mathbf{x}_i, \gamma_1(d(\mathbf{x}_i), \phi(\mathbf{x}_i))), i = 1, 2, \dots, T\} \quad (7)$$

where T is the number of locations in the RSRP radio map \mathcal{M} . It is evident that the elements in standard RSRP radio maps and those in the PAM do not correspond one-to-one. Specifically, the PAM serves as a sparse representation of conventional RSRP radio maps, significantly reducing space complexity by leveraging the uniform horizontal gain of antennas.

Assuming the measurement locations in a RSRP radio map \mathcal{M} are continuous, Algorithm 1 are utilized to construct the PAM Γ from \mathcal{M} . The inputs, *i.e.*, M and N , of Algorithm 1 depend on the requirements of PAM resolution. Larger M and N contribute to more refined propagation pattern.

Algorithm 1 PAM Construction

Input: Number of columns M , and number of rows N of Γ .
Objective: PAM matrix Γ

- 1) Filter out all the LOS positions $\mathbf{x}_i \in \mathcal{D}_0 \cap \mathcal{M}$ for $i \in \{1, 2, \dots, T\}$.
- 2) Calculate the range of distances $d(\mathbf{x}_i)$ and the range of elevation angles $\phi(\mathbf{x}_i)$ for $\forall \mathbf{x}_i \in \mathcal{D}_0 \cap \mathcal{M}$.
- 3) Generate a monotonically increasing arithmetic sequence $\{d_1, d_2, \dots, d_M\}$ with $d_1 = \min_{\mathbf{x}_i \in \mathcal{D}_0 \cap \mathcal{M}} \{d(\mathbf{x}_i)\}$, $d_M = \max_{\mathbf{x}_i \in \mathcal{D}_0 \cap \mathcal{M}} \{d(\mathbf{x}_i)\}$.
- 4) Generate a monotonically increasing arithmetic sequence $\{\phi_1, \phi_2, \dots, \phi_N\}$ with $\phi_1 = \min_{\mathbf{x}_i \in \mathcal{D}_0 \cap \mathcal{M}} \{\phi(\mathbf{x}_i)\}$, $\phi_N = \max_{\mathbf{x}_i \in \mathcal{D}_0 \cap \mathcal{M}} \{\phi(\mathbf{x}_i)\}$.
- 5) Generate a matrix Γ according to (6).

B. LOS Detection

Step 1 in Algorithm 1 requires the detection of LOS and NLOS positions of the UAV. If the 3D city maps are available, one can directly apply analytical geometric methods to detect whether the line between the UAV at the position \mathbf{x} and the transmitter at the position \mathbf{u} is blocked by buildings.

Without the need to construct a city map, one can apply the maximum likelihood estimation method to the channel path loss measurements. Denote $f_k(x)$ as the probability density function of the random variable ξ_k for $k \in \{0, 1\}$ in the channel model (2). If the RSRP measurement $\gamma(\mathbf{x}, \phi(\mathbf{x}))$ is observed at the UAV position \mathbf{x} , one can pick the k^* that maximizes the likelihood function, *i.e.*, $k^* = \arg\max_{k \in \{0, 1\}} f_k(\gamma(\mathbf{x}, \phi(\mathbf{x})) - (p_t + a(\phi(\mathbf{x})) - \alpha_k - \beta_k \log_{10}(d(\mathbf{x}))))$.

In particular, ξ_k for $k \in \{0, 1\}$ is assumed to be a zero-mean Gaussian random variable with variance σ_k^2 . Then, the detection rule is equivalent to $k^* = \arg\max_{k \in \{0, 1\}} |\gamma(\mathbf{x}, \phi(\mathbf{x})) - (p_t + a(\phi(\mathbf{x})) - \alpha_k - \beta_k \log_{10}(d(\mathbf{x})))| / \sigma_k$.

Here, the channel parameters α_k and β_k for $k \in \{0, 1\}$ can be set using experience values such as path loss parameters in 3GPP models [9]. The transmit power p_t is easily obtained by spectrum analyzer or accurate signal source. However, the relative antenna gain $a(\phi(\mathbf{x}))$ is unknown. To address this issue, one may need to choose a proper value of $a(\phi(\mathbf{x}))$. In Section IV, we set $a(\phi(\mathbf{x}))$ to 0. This strategy works because the difference of the channel gain between LOS links and NLOS links is relatively large compared with the antenna gain variation.¹

C. PAM Completion

In practice, the matrix Γ , containing RSRP measurements at discrete propagation distances and elevation angles, may have missing values at certain distances due to the limited number of LOS measurements. To address this issue, we employ a

¹For example, the channel parameters α_0 , β_0 , α_1 , and β_1 are given by 22, 28, 22.7, and 36.7, respectively [9]. Then, the difference of the channel gain between LOS links and NLOS links are 18.1 dB at a propagation distance of 100 meters while the antenna gain variation of antennas is typically 5 dBi.

matrix completion technique based on weighted KNN for PAM completion.

Specifically, for a missing value at the position (n, m) in matrix Γ , the estimated value $\hat{\Gamma}_{nm}$ is calculated as:

$$\hat{\Gamma}_{nm} = \frac{\sum_{(k,j) \in \text{KNN}(n,m)} w_{nm}(k,j) \cdot \Gamma_{kj}}{\sum_{(k,j) \in \text{KNN}(n,m)} w_{nm}(k,j)} \quad (8)$$

where $\text{KNN}(n, m)$ represents the indices of K -nearest neighbors to position (n, m) , $w_{nm}(k, j)$ is the weight assigned to the neighbor at the position (k, j) based on its similarity to the position (n, m) , and Γ_{kj} is the observed RSRP measurement at position (k, j) . The modified Epanechnikov Kernel is adopted as the weights $w_{nm}(k, j)$, which adds different scaling factors to the weights of the row and column averages. Therefore, the characteristics of the existing data can be thoroughly exploited to achieve optimal completion.

By applying KNN-based matrix completion, the completeness of the RSRP measurements in Γ is enhanced, ensuring a more comprehensive representation of the signal propagation environment across different distances and elevation angles.

D. Antenna Pattern Reconstruction with Low-rank Properties

To exploiting the inherent properties of the PAM matrix Γ , SVD is employed due to its ability to separate a complex matrix into simpler, interpretable components.

The PAM matrix Γ is decomposed by SVD as

$$\Gamma = \mathbf{U} \sqrt{\Sigma} \sqrt{\Sigma} \mathbf{V}^T \quad (9)$$

where \mathbf{U} and \mathbf{V} are orthogonal matrices containing the left and right singular vectors, respectively, and Σ is a diagonal matrix containing the singular values. Specifically, define $\mathbf{A} = \mathbf{U} \sqrt{\Sigma}$, and $\mathbf{G} = \sqrt{\Sigma} \mathbf{V}^T$. Then, $\Gamma = \mathbf{A} \mathbf{G}$.

Through numerical analysis, it is observed that the power angular map Γ typically exhibits low rank properties. Fig. 2 shows the normalized Frobenius norm error for various low-rank approximations of the PAM matrix Γ constructed from the real-world measurements. By truncating Σ and retaining only the first k singular values, we can construct a series of low-rank approximations Γ_k . The normalized Frobenius norm error, defined as $\|\Gamma - \Gamma_k\|_F / \|\Gamma\|_F$, quantifies the difference between the original matrix Γ and its low-rank approximation Γ_k . It is observed that the dominant singular value only corresponds to a normalized Frobenius norm error of about 0.04, and the additional singular values contribute less to the overall structure of the matrix.

To extract the antenna pattern denoted as $\mathbf{a} = [a_1(\phi_1), a_1(\phi_2), \dots, a_1(\phi_N)]^T$, it suffices to use the first column of \mathbf{U} , which corresponds to the largest singular value. Therefore, the reconstructed antenna gain $\hat{\mathbf{a}} = [\hat{a}_1(\phi_1), \hat{a}_1(\phi_2), \dots, \hat{a}_1(\phi_N)]^T$ is given by

$$\hat{\mathbf{a}} = Z_a \mathbf{u}_1 \sqrt{\Sigma_1} \quad (10)$$

where \mathbf{u}_1 is the first column of \mathbf{U} , Σ_1 is the largest singular value, and Z_a is a scaling factor to scale the range of $\hat{\mathbf{a}}$ to the actual range of \mathbf{a} such that $\min\{\hat{\mathbf{a}}\} = \min\{\mathbf{a}\}$ and

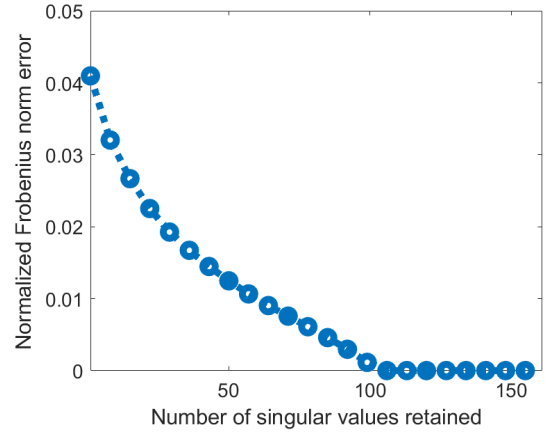


Figure 2. Normalized Frobenius norm error for various low-rank approximations of Γ constructed from real-world measurements

$\max\{\hat{\mathbf{a}}\} = \max\{\mathbf{a}\}$. Here, the transmit power p_t is absorbed into the singular values and the left and right singular vectors, simplifying our analysis.

Similarly, the channel gain pattern w.r.t. the propagation distance, denoted as $\mathbf{g} = [g_1(d_1), g_1(d_2), \dots, g_1(d_M)]^T$, is obtained using the first column of \mathbf{V} . Thus, the reconstructed channel gain map $\hat{\mathbf{g}} = [\hat{g}_1(d_1), \hat{g}_1(d_2), \dots, \hat{g}_1(d_M)]^T$ is given by

$$\hat{\mathbf{g}} = Z_g \mathbf{v}_1 \sqrt{\Sigma_1}. \quad (11)$$

where \mathbf{v}_1 is the first column of \mathbf{V} , Σ_1 is the largest singular value, and Z_g is a scaling factor to scale the range of $\hat{\mathbf{g}}$ to the actual range of \mathbf{g} such that $\min\{\hat{\mathbf{g}}\} = \min\{\mathbf{g}\}$ and $\max\{\hat{\mathbf{g}}\} = \max\{\mathbf{g}\}$.

The theoretical underpinning of using the first singular vectors \mathbf{u}_1 and \mathbf{v}_1 lies in the Eckart-Young theorem, which states that the best low-rank approximation of a matrix in terms of the Frobenius norm is obtained by truncating the SVD to the largest singular values and their corresponding singular vectors. Hence, by focusing on the largest singular value and its associated vectors, we ensure that the most significant patterns in Γ are preserved, providing an accurate approximation of the antenna and channel gains.

IV. EXPERIMENTS

The experiments are conducted both on simulated data and real-world measurements for the evaluation of the performance of the proposed scheme.

A. Experiment Settings

1) *Simulation settings*: The transmitter is equipped with an omnidirectional antenna while the UAV is equipped with a half-dipole antenna. The antenna data is generated by Wireless Insite[®] which provides 3D ray-tracing for the analysis of site-specific radio wave propagation and wireless communication

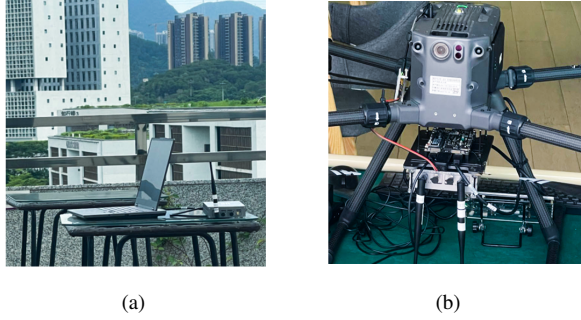
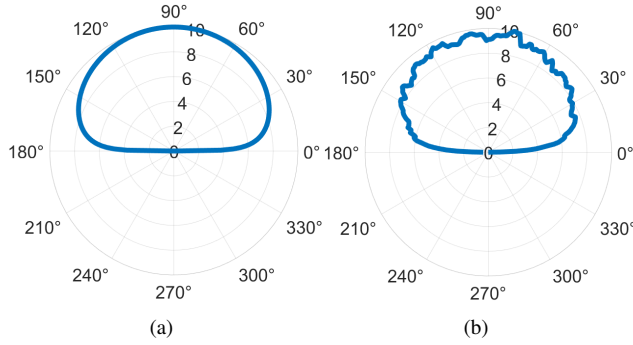


Figure 3. (a) The ground transmitting system (b) The air receiving system

Figure 4. (a) Theoretical pattern of a half-wave dipole antenna. (b) Reconstructed antenna pattern with $N = 180$.

systems. The transmit power p_t is set as 0 dBm. According to [9], the channel model in (2) is specified as

$$g(\mathbf{x}) = \begin{cases} 22 + 28 \log_{10}(\|\mathbf{x} - \mathbf{u}\|_2) + \xi_0 & \text{if } \mathbf{x} \in \mathcal{D}_0 \\ 22.7 + 36.7 \log_{10}(\|\mathbf{x} - \mathbf{u}\|_2) + \xi_1 & \text{otherwise} \end{cases} \quad (12)$$

where the standard variance σ_0 of ξ_0 is set as 2 dB, and the standard variance σ_1 of ξ_1 is set as 5 dB.

2) *Real-world experiment*: The air-ground communication system consists of a ground transmitting system and an air receiving system as shown in Fig. 3. The transmitter consists of a laptop and a Universal Software Radio Peripheral (USRP) B210, and a VERT 2450 antenna. The laptop generates the signal, and processes the signal using GNU Radio while the USRP with the VERT 2450 antenna sends the signal. The receiver consists of a Matrice 300 RTK UAV, a LattePanda single board computer, a USRP B210, and two VERT 2450 antennas. The USRP with the VERT 2450 antennas receives the signal, and the single board computer processes the signal, and generate a RSRP map $\mathcal{M} = \{(\mathbf{x}_i, \gamma_i(d(\mathbf{x}_i), \phi(\mathbf{x}_i))), i = 1, 2, \dots, T\}$.

B. Antenna Pattern Reconstruction of a Half-wave Dipole Antenna

Fig. 4 shows comparison between the actual antenna pattern and the reconstructed antenna pattern of a half-wave dipole antenna under the setting of $N = 180$. It is found that the reconstructed antenna radiation pattern is quite close to the

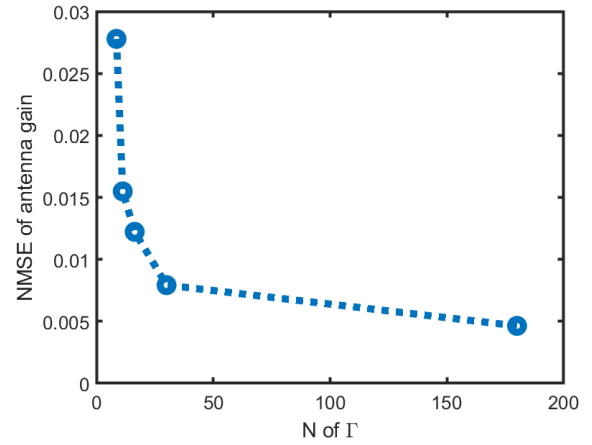
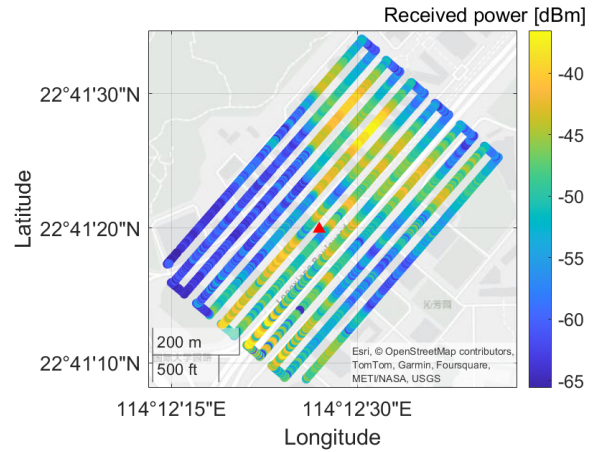
Figure 5. NMSE of the reconstructed antenna gain under different values of N of Γ .

Figure 6. RSRP map from real-world measurements

actual one of a half-wave dipole antenna although there are some measurement noise.

Additionally, define the NMSE of the reconstructed antenna pattern as

$$\text{NMSE}(\hat{\mathbf{a}}) = \frac{\|\mathbf{a} - \hat{\mathbf{a}}\|_2^2}{\|\mathbf{a}\|_2^2}. \quad (13)$$

Fig. 5 shows the NMSE of the reconstructed antenna pattern under different settings of N . It is observed that the NMSE of the reconstructed antenna gain decreases w.r.t. the increase of the numbers of elevation angles, *i.e.*, N of Γ . Only 30 elevation angle measurements are necessary to achieve a NMSE of less than 0.01 for the reconstructed antenna pattern.

C. Antenna Pattern Reconstruction Using Outdoor Measurements

Fig. 6 shows the RSRP map constructed using the outdoor signal data measured by the air-ground communication system. It is observed that the measurements are obtained along the UAV trajectory. Even though the transmitter is placed on the top of a building in the area of interest, there are still some

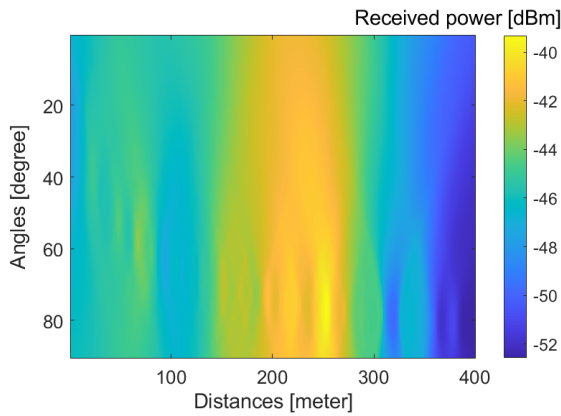


Figure 7. KNN-augmented PAM

higher buildings which block the propagation path during the flight. As shown in Fig. 6, the RSRP in the NLOS region is quite low. Since the measurements are discrete, and the NLOS region exists, the number of LOS measurements are limited. After implementing the LOS detection, 758 measurements are classified as LOS measurements available for constructing the PAM matrix Γ with $N = 90$ and $M = 400$. Hence, the percentage of missing data is about 97.9%. The KNN-augmented PAM is shown in Fig. 7. It is observed that the KNN-augmented PAM demonstrates the RSRP is not monotonically decreasing w.r.t. the distance because of the irregular antenna pattern.

Fig. 8 shows the reconstructed antenna pattern of the VERT 2450 antenna. Since the antenna of the transmitter is pointing upward and the antenna of the receiver is pointing downward, the reconstructed antenna pattern of one VERT 2450 is given by $\hat{\alpha}/2$. As the measurements only correspond to the elevation angles ranging from $[0, 90)$, the antenna pattern in the elevation angles ranging from $(270, 360]$ is symmetrically generated according to that in $[0, 90)$. It is observed from Fig. 8(b) that the reconstructed antenna pattern has a similar distribution to that of the VERT 2450 in the datasheet² as shown in Fig. 8(a). Possible errors originate from manufacturing errors of the tested VERT 2450 antennas, insufficient measurement data, insufficient measurement accuracy, Doppler effect, etc. The true antenna patterns may require future calibration in a professional microwave anechoic chamber.

V. CONCLUSION

In conclusion, this study validates the feasibility of reconstructing antenna radiation patterns using outdoor signal strength measurements, bypassing the need for specialized anechoic or reverberation chambers. By utilizing sparse RSRP measurements, we effectively constructed a 2D power angular map that captures the essential characteristics of the

²The datasheet can be accessed online at https://kb.ettus.com/images/9/9e/ettus_research_vert2450_datasheet.pdf. [Accessed: 31-May-2024].

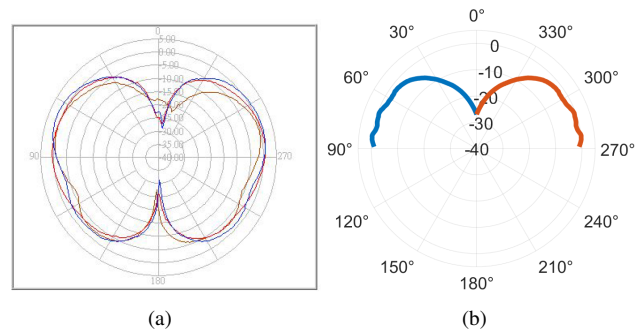


Figure 8. (a) Antenna pattern of VERT 2450 from the data sheet of VERT 2450. The red line indicates the antenna pattern under the carrier frequency of 2450 MHz. (b) Reconstructed antenna pattern under the carrier frequency of 2450 MHz.

antenna's radiation pattern. The use of a weighted KNN-based matrix completion method and SVD allowed for imputation of missing values and separation of antenna gain from path loss. Experimental results, confirmed through simulations and real-world measurements, showed that only 30 elevation angle measurements are necessary to achieve a NMSE of less than 0.01 for the reconstructed antenna pattern. The reconstructed radiation pattern for the VERT 2450 antenna, has a similar distribution to that in the datasheet, highlights the practicality and cost-effectiveness of our approach for antenna pattern reconstruction in outdoor settings. Future extensions of this work may incorporate azimuth angles using tensor methods to capture horizontal patterns more comprehensively.

REFERENCES

- [1] J. Zheng, X. Chen, and Y. Huang, "An effective antenna pattern reconstruction method for planar near-field measurement system," *IEEE Trans. Instrum. Meas.*, vol. 71, pp. 1–12, 2022.
- [2] J. Puškely and Z. Nováček, "Reconstruction of antenna radiation pattern at 310 ghz using image compression methods," in *Proc. Eur. Conf. Antennas Propag. (EuCAP)*, 2010, pp. 1–5.
- [3] Q. Xu, Y. Huang, L. Xing, C. Song, Z. Tian, S. S. Aljaafreh, and M. Stanley, "3-D antenna radiation pattern reconstruction in a reverberation chamber using spherical wave decomposition," *IEEE Trans. Antennas Propag.*, vol. 65, no. 4, pp. 1728–1739, 2017.
- [4] J. Zheng, W. Xue, X. Liu, and X. Chen, "Antenna radiation pattern reconstruction based on spherical wave decomposition in imperfect reverberation chamber," in *Proc. IEEE Int. Conf. Electron. Inf. Commun. Technol. (ICEICT)*, 2021, pp. 471–476.
- [5] J. Zheng, X. Chen, X. Liu, M. Zhang, B. Liu, and Y. Huang, "An improved method for reconstructing antenna radiation pattern in a loaded reverberation chamber," *IEEE Trans. Instrum. Meas.*, vol. 71, pp. 1–12, 2022.
- [6] J. Koh, A. De, T. K. Sarkar, H. Moon, W. Zhao, and M. Salazar-Palma, "Free space radiation pattern reconstruction from non-anechoic measurements using an impulse response of the environment," *IEEE Trans. Antennas Propag.*, vol. 60, no. 2, pp. 821–831, 2012.
- [7] Z. Wang, C. Pang, Y. Li, and X. Wang, "A method for radiation pattern reconstruction of phased-array antenna," *IEEE Trans. Antennas Propag. Lett.*, vol. 19, no. 1, pp. 168–172, 2020.
- [8] Y. Miao and J.-i. Takada, "Antenna pattern reconstruction by spherical vector waves for spherical antenna measurement," in *Proc. Int. Symp. Electromagn. Theory*, 2013, pp. 1035–1038.
- [9] J. Chen, U. Mitra, and D. Gesbert, "3D urban UAV relay placement: Linear complexity algorithm and analysis," *IEEE Trans. on Wireless Commun.*, vol. 20, no. 8, pp. 5243–5257, 2021.